Eco-Environment & Health 3 (2024) 466–475

Contents lists available at ScienceDirect

Eco-Environment & Health

journal homepage: www.journals.elsevier.com/eco-environment-and-health

Original Research Article

Effects of 3D microstructure of porous media on DNAPL migration and remediation by surface active agents in groundwater

Zhou Cheng [a,b], Ming Wu [a,*], Yanru Hao [a], Cehui Mo [a], Qusheng Li [c], Jianfeng Wu [d], Jichun Wu [d], Bill X. Hu [e], Guoping Lu [a]

[a] Guangdong Provincial Research Center for Environment Pollution Control and Remediation Materials, College of Life Science and Technology, Jinan University, Guangzhou 510632, China
[b] Guangdong Provincial Academy of Environmental Science, Guangzhou 510045, China
[c] Guangdong Key Laboratory of Environmental Pollution and Health, School of Environment, Jinan University, Guangzhou 510632, China
[d] Key Laboratory of Surficial Geochemistry, Ministry of Education, Department of Hydrosciences, School of Earth Sciences and Engineering, Nanjing University, Nanjing 210023, China
[e] School of Water Conservancy and Environment, University of Jinan, Jinan 250022, China

ARTICLE INFO

Keywords:
Porous media
Sequential gaussian simulation (SGS)
Regular tetrahedron microstructure (RTM)
Right square pyramid microstructure (RSPM)
Surfactant-enhanced aquifer remediation (SEAR)

ABSTRACT

Aquifers composed of porous granular media are important to human beings because they are capable of storing a large amount of groundwater. Contaminant migration and remediation in subsurface environments are strongly influenced by three-dimensional (3D) microstructures of porous media. In this study, fractal models are developed to investigate contaminant transport and surfactant-enhanced aquifer remediation (SEAR) for the regular tetrahedron microstructure (RTM) and right square pyramid microstructure (RSPM). The relationships of permeability and entry pressure are derived for these two kinds of 3D microstructures of granular porous media. Afterward, the difference in perchloroethylene (PCE) migration and SEAR efficiency between RTM and RSPM is investigated by the numerical simulation based on a synthetic heterogeneous granular aquifer. Results indicate that PCE penetrates faster and spreads farther in RSPM-based aquifers compared with RTM-based aquifers. Further, SEAR in RTM-based aquifers can achieve remediation efficiencies of 66.129%–92.214% with a mean of 84.324%, which is clearly lower than the SEAR efficiency of 70.149%–94.773% (with a mean of 89.122%) in RSPM-based aquifers. Findings are significant for understanding the 3D microstructure of porous media and how the microstructure of porous media affects macroscopic contaminant behaviors and remediation.

1. Introduction

In addition to being one of the world's most valuable freshwater resources, groundwater is also a primary source of domestic drinking water for over half the world's population [1–11]. In recent years, however, more and more contaminants have been released into the subsurface environment, especially organic contaminants released from industrial emissions and leaks, such as underground storage tank spills [12–20]. The issue of groundwater contamination has become a major environmental concern [14,21–31]. The dense non-aqueous phase liquid (DNAPL) detected in groundwater is toxic, carcinogenic, teratogenic, and mutagenic, posing serious health risks to humans and the environment [29,32,33]. When DNAPL enters the aquifer from an underground storage tank, it can form residual ganglia and contaminant pools, serving as long-term contamination sources [34–39]. Therefore, groundwater restoration and subsurface environment improvement depend on the investigation of DNAPL migration and remediation in aquifers.

Various transport characteristics are closely controlled by the microstructure of materials, including hydraulic conductivity, diffusivity, and dispersivity [15,19,40–45], which can strongly affect macroscopic DNAPL migration and remediation in porous media. Consequently, numerous researchers have examined how material microstructure affects macroscopic properties. Microscale geometric structure, for instance, plays a key role in determining the permeability K in Kozeny-Carman equation relating to Kozeny constant c [44,46,47]. As a result of the development of fractal theory, natural porous media can be viewed as fractal objects and investigated by means of fractal analysis [48–51]. For porous media, various geometrical models of microstructure have been developed to study thermal conductivity, tortuosity, permeability, and fluid invasion, all of which are useful for obtaining

* Corresponding author.
E-mail address: wumingnj@foxmail.com (M. Wu).

https://doi.org/10.1016/j.eehl.2024.08.003
Received 19 July 2023; Received in revised form 21 July 2024; Accepted 21 August 2024
Available online 30 August 2024

mathematical models of macroscopic parameters [52–55]. Microstructure, however, was overly idealized in previous fractal models. Based on two-dimensional (2D) porous media containing spherical particles, Yu and Cheng [52] developed a simple model to quantify tortuosity and permeability. A fractal method was used to derive the physical properties of porous media with two phases and the invasion depth of extraneous fluids [47,53,54,56]. To estimate REV and investigate contaminant transport in porous media, various 2D microstructure models were developed by analyzing grain geometry and microarrangements of solid particles. In previous studies, material microstructures were usually two-dimensional, and their influence on contaminants behaviors was sparsely investigated [52–54,57–59].

The study examines the effects of microstructures on macroscopic DNAPL migration and remediation using granular porous media with regular tetrahedron microstructure (RTM) and right square pyramid microstructure (RSPM). In these two kinds of 3D microstructures, fractal models are developed to determine permeability and entry pressure mathematically. Subsequently, 200 realizations of underground storage tank spill-contaminated sites are generated using a sequential Gaussian simulation (SGS). Perchloroethylene (PCE) migration and remediation by surfactant-enhanced aquifer remediation (SEAR) are simulated using UTCHEM. Based on simulated results, the effect of microstructures on DNAPL transport and SEAR efficiency is compared between RTM and RSPM.

2. Methodology

2.1. Microscale fractal models of granular porous media

The fractal theory suggests that porous media containing numerous pores can be viewed as a bundle of capillary tubes. An infinitesimal element (unit element) consisting of tortuous capillary tubes is selected from the porous media. There is a relationship between the tortuous length of a capillary tube and its diameter:

$$L_t(\lambda) = \lambda^{1-D_T} L_s^{D_T} \tag{1}$$

where λ, L_t, and L_S are the diameter, the tortuous length, and the straight length of the capillary tube, respectively; D_T is the fractal dimension of tortuosity.

Yu and Cheng [52] found that the cumulative number of capillary tubes in a unit element can be derived as follows:

$$\mathrm{N}(L \geq \lambda) = \left(\frac{\lambda_{\max}}{\lambda}\right)^{D_f} \tag{2}$$

where D_f is the fractal dimension for pore/capillary areas in infinitesimal element; $\lambda_{\max}$ is the maximum value of capillary tube diameter.

Afterward, the derivative of Eq. 2 can be achieved:

$$-\mathrm{d}N = D_f \lambda_{\max}^{D_f} \lambda^{-(D_f+1)} \mathrm{d}\lambda \tag{3}$$

The total number of capillary tubes in infinitesimal element is calculated by integrating Eq. 3 from $\lambda_{\min}$ (the minimum diameter of capillary tubes) to $\lambda_{\max}$:

$$N_t(L \geq \lambda_{\min}) = \left(\frac{\lambda_{\max}}{\lambda_{\min}}\right)^{D_f} \tag{4}$$

Substituting Eq. 4 into Eq. 3 results in:

$$-\frac{\mathrm{d}N}{N_t} = D_f \lambda_{\min}^{D_f} \lambda^{-(D_f+1)} \mathrm{d}\lambda = f(\lambda)\mathrm{d}\lambda \tag{5}$$

where $f(\lambda) = D_f \lambda_{\min}^{D_f} \lambda^{-(D_f+1)}$ is the function of probability density. If $\left(\frac{\lambda_{\min}}{\lambda_{\max}}\right)^{D_f} = 0$, $\int_{-\infty}^{+\infty} f(\lambda)\mathrm{d}\lambda = \int_{\lambda_{\min}}^{\lambda_{\max}} f(\lambda)\mathrm{d}\lambda = 1 - \left(\frac{\lambda_{\min}}{\lambda_{\max}}\right)^{D_f} = 1$.

Assume the flow path is L_t, and that the pressure difference between the inlet and outlet is ΔP. The viscosity of fluid is μ. According to Poiseuille equation, the flow rate of an individual capillary tube (q) is given by:

$$q = \frac{\pi r^4 \Delta P}{8\mu L} = \frac{\pi\left(\frac{\lambda}{2}\right)^4 \Delta P}{8\mu L} = \frac{\pi\lambda^4 \Delta P}{128\mu L} \tag{6}$$

The derivative of the flow rate of an individual capillary tube (q) is:

$$\mathrm{d}q = [-\mathrm{d}N]\frac{\pi\lambda^4 \Delta P}{128\mu L}$$

$$= \frac{\pi}{128}\frac{\Delta P}{\mu}\frac{D_f \lambda_{\max}^{D_f}}{L_0^{D_T}} \lambda^{2+D_T-D_f} \mathrm{d}\lambda \tag{7}$$

The total flow rate (Q) can be obtained by integrating q from $\lambda_{\min}$ to $\lambda_{\max}$:

$$Q = \int \mathrm{d}\lambda$$

$$= \int_{\lambda_{\min}}^{\lambda_{\max}} \frac{\pi}{128}\frac{\Delta P}{\mu}\frac{D_f \lambda_{\max}^{D_f}}{L_0^{D_T}} \lambda^{2+D_T-D_f} \mathrm{d}\lambda \tag{8}$$

$$= \frac{\pi}{128}\frac{\Delta P}{\mu}\frac{D_f}{3+D_T-D_f}\frac{1}{L_0^{D_T}} \lambda_{\max}^{3+D_T}\left[1 - \left(\frac{\lambda_{\min}}{\lambda_{\max}}\right)^{D_f}\left(\frac{\lambda_{\min}}{\lambda_{\max}}\right)^{3+D_T-D_f}\right]$$

Due to $1 < D_T < 2$, $1 < D_f < 2$ and $(3 + D_T - 2D_f) > 0$, then $\left(\frac{\lambda_{\min}}{\lambda_{\max}}\right)^{D_f} \cong 0$, $0 < \left(\frac{\lambda_{\min}}{\lambda_{\max}}\right)^{3+D_T-D_f} < 1$. Afterward, Eq. 8 can be simplified to:

$$Q = \frac{\pi}{128}\frac{\Delta P}{\mu}\frac{D_f}{3+D_T-D_f}\frac{1}{L_0^{D_T}} \lambda_{\max}^{3+D_T} \tag{9}$$

The permeability can be derived using Darcy's law $Q = \frac{kA\triangle P}{\mu L_0}$:

$$k = \frac{\pi}{128}\frac{D_f}{3+D_T-D_f}\frac{L_0^{1-D_T}}{A} \lambda_{\max}^{3+D_T} \tag{10}$$

The tortuosity equals to the ratio of the tortuous length of flow path to the straight length of flow path [15,44,60,61]. Substituting Eq. 1, the tortuosity is given by [40]:

$$\tau = \frac{L_t(\lambda)}{L_S} = \left(\frac{L_s}{\lambda}\right)^{D_t-1} \tag{11}$$

$$D_t = 1 + \frac{\ln \tau}{\ln \frac{L_s}{\lambda}} \tag{12}$$

Two kinds of 3D microstructure of granular porous media are shown in Figs. S1a–d. A regular tetrahedron and right square pyramid are selected from the 3D microstructure of granular porous media as unit cells. RTM is composed of four solid particles (Fig. S1a), and its bottom is a regular triangle (Fig. S1b), while RSPM is composed of five solid particles (Fig. S1c), and its bottom is square (Fig. S1d). For the RTM in Fig. S1a, the porosity is:

$$n = \frac{V_t - \frac{4}{15}\pi R_v^3}{V_t} \tag{13}$$

where V_t is the total volume of RTM; R_v is the median radius of solid particles. The total volume of RTM can be obtained from Eq. 13:

$$V_t = \frac{4\pi R_v^3}{15(1-n)} \tag{14}$$

Simultaneously, the volume of RTM also can be calculated by the side length of RTM (L_{tl}):

$$V_t = \frac{\sqrt{2}}{12} L_{tl}^3 \tag{15}$$

$$L_{tl} = R_v \sqrt{\frac{8\sqrt{2}\pi}{5(1-n)}} \tag{16}$$

Consequently, the pore volume in RTM (V_{tp}) is given by:

$$V_{tp} = V_t - \frac{4}{15}\pi R_v^3 = \frac{4\pi R_v^3 n}{15(1-n)} \tag{17}$$

Approximating the irregular pore as a sphere, we can derive the diameter of the sphere (λ_{t1}):

$$V_{tp} = \frac{4}{3}\pi\left(\frac{\lambda_{tl}}{2}\right)^3 \tag{18}$$

$$\lambda_{tl} = 2R_v \sqrt[3]{\frac{n}{5(1-n)}} \tag{19}$$

The bottom plane of RTM is a regular triangle composed of three solid particles, as shown in Fig. S1b. The area of the regular triangle (A_{tb}) and the area of solid particles (A_{tbs}) respectively are:

$$A_{tb} = \frac{\sqrt{3}}{4} L_{tl}^2 \tag{20}$$

$$A_{tbs} = \frac{1}{2}\pi R_v^2 \tag{21}$$

Then the area of pore in the bottom regular triangle (A_{tbp}) is:

$$A_{tbp} = \frac{\sqrt{3}}{4} L_{tl}^2 - \frac{1}{2}\pi R_v^2 \tag{22}$$

By approximating the irregular pore in the bottom regular triangle as a circle, its diameter (λ_{t2}) can be calculated:

$$A_{tbp} = \pi\left(\frac{\lambda_{t2}}{2}\right)^2 \tag{23}$$

$$\lambda_{t2} = 2\sqrt{\frac{A_{tbp}}{\pi}} \tag{24}$$

In RTM, the gap length (ΔL_{tl}) between the adjacent particles is given by:

$$\Delta L_{tl} = L_{tl} - 2R_v = R_v\left[\sqrt[3]{\frac{8\sqrt{2}\pi}{5(1-n)}} - 2\right] \tag{25}$$

The average diameter length of the capillary tubes in RTM (λ_{tl}) is quantified as:

$$\lambda_{tl} = \frac{\lambda_{t1} + \lambda_{t2} + \Delta L_{tl}}{3} \tag{26}$$

Simultaneously, the side length of the regular tetrahedron in Fig. S1a is $L_{tl} = 2R_v + \Delta L_{tl}$. Accordingly, the total volume of the regular tetrahedron in RTM microstructure is $V_t = \frac{\sqrt{2}}{12}L_{tl}^3 = \frac{\sqrt{2}}{12}(2R_v + \Delta L_{tl})^3$, and the inner pore volume is $V_{tp} = V_t - \frac{4}{15}\pi R_v^3 = \frac{\sqrt{2}}{12}(2R_v + \Delta L_{tl})^3 - \frac{4}{15}\pi R_v^3$. As a result, the porosity of RTM is expressed as:

$$n = \frac{V_{tp}}{V_t} = \frac{\frac{\sqrt{2}}{12}(2R_v + \Delta L_{tl})^3 - \frac{4}{15}\pi R_v^3}{\frac{\sqrt{2}}{12}(2R_v + \Delta L_{tl})^3} \tag{27}$$

Based on Eq. 28, the ratio $p_1 = \Delta L_{tl}/R_v$ can be obtained:

$$p_1 = \frac{d}{R_v} = 2\sqrt{\frac{\sqrt{2}\pi}{5(1-n)}} - 2 \tag{28}$$

The tortuosity of RTM can be determined based on the ratio $p_1 = \Delta L_{tl}/R_v$ of RTM and the expression of tortuosity 3D microstructure [44]:

$$\tau = \frac{\tau_1 + \tau_2}{2} \tag{29}$$

where $\tau_1 = 1 + \frac{\pi-2}{\frac{4\pi}{3(1-n)} + \left[\frac{4\pi}{3(1-n)}\right]^{1/3} - 2\left[\frac{4\pi}{3(1-n)}\right]^{2/3}}$, and $\tau_2 = \frac{6\sqrt{3p_1^2+12p_1+8} - (3p_1^2+12p_1+4)arcsin\frac{2}{\sqrt{3}(p_1+2)} - 6(p+2)^2 arctg\frac{-2}{\sqrt{3p_1^2+12p_1+8}}}{8\sqrt{3}(p_1+2)}$.

According to the theory of the Sierpinkski gasket (Fig. S2), the dimensionless pore volume of the regular tetrahedron in RTM microstructure (Fig. S1a) is given by:

$$V_{tp} = \left(L_{tl}^+\right)^{D_f} \tag{30}$$

where $L_{tl}^+ = L_{tl}/d_{\min}$; $d_{\min}$ is the minimum diameter of solid particles.

Solve Eq. 30 and the D_f can be achieved:

$$D_f = \frac{\ln V_{tp}}{\ln L_{tl}^+} \tag{31}$$

The dimensionless total volume of the regular tetrahedron in RTM (V_t^+) is given by:

$$V_t^+ = \frac{V_t}{V_{sp}} \tag{32}$$

where V_{sp} is the minimum volume of solid particles, $V_{sp} = \frac{4}{3}\pi\left(\frac{d_{\min}}{2}\right)^3 = \frac{1}{6}\pi d_{\min}^3$.

The dimensionless total volume of the regular tetrahedron in RTM (V_t^+) can be written as:

$$V_t^+ = \left(L_{tl}^+\right)^3 V_t^+ = \left(L_{tl}^+\right)^3 \tag{33}$$

Afterward, L_{tl}^+ is calculated as:

$$L_{tl}^+ = \sqrt[3]{V_t^+} = d^+ \sqrt[3]{\frac{1}{5(1-n)}} \tag{34}$$

where $d^+ = \frac{2R_v}{d_{\min}}$. According to Yu and Cheng [52], the value of d^+ is set as 18 or 24.

Consequently, the D_f of RTM is derived as:

$$\begin{aligned} D_f &= \frac{\ln V_{tp}}{\ln L_{tl}^+} = \frac{\ln\left(V_t^+ n\right)}{\ln \sqrt[3]{V_t^+}} \\ &= 3 + \frac{\ln n}{\ln L_{tl}^+} \\ &= 3 + \frac{\ln n}{\ln\left[d^+ \sqrt[3]{\frac{1}{5(1-n)}}\right]} \end{aligned} \tag{35}$$

For the RSPM in Fig. S1c, its porosity is given by:

$$n = \frac{V_r - \frac{4}{9}\pi R_v^3}{V_r} \tag{36}$$

where V_r is the volume of RSPM. Then the volume of RSPM can be obtained from Eq. 36:

$$V_r = \frac{4\pi R_v^3}{9(1-n)} \tag{37}$$

Simultaneously, the volume of RTM can also be calculated by the side length of RSPM (L_{rl}):

$$V_t = \frac{\sqrt{2}}{6} L_{rl}^3 \tag{38}$$

$$L_{rl} = R_v \sqrt[3]{\frac{8\pi}{3\sqrt{2}(1-n)}} \tag{39}$$

Consequently, the pore volume in RSPM is given by:

$$V_{rp} = V_r - \frac{4}{9}\pi R_v^3 = \frac{4\pi R_v^3 n}{9(1-n)} \tag{40}$$

By approximating the irregular pore in RSPM as a sphere, its diameter (λ_{r1}) can be calculated:

$$V_{rp} = \frac{4}{3}\pi\left(\frac{\lambda_{rl}}{2}\right)^3 \tag{41}$$

$$\lambda_{rl} = 2R_v \sqrt[3]{\frac{n}{3(1-n)}} \tag{42}$$

The bottom plane of RSPM is square composed of four solid particles (Fig. S1d). The area of the square (A_{rb}) and the area of solid particles (A_{rbs}) respectively are expressed as:

$$A_{rb} = L_r^2 \tag{43}$$

$$A_{rbs} = \pi R_v^2 \tag{44}$$

Then, the area of pore in the bottom square of RSPM (A_{rbp}) can be obtained:

$$A_{rbp} = L_r^2 - \pi R_v^2 \tag{45}$$

By approximating the irregular pore in the bottom square of RSPM as a circle, its diameter (λ_{r2}) can be calculated:

$$A_{rbp} = \pi\left(\frac{\lambda_{r2}}{2}\right)^2 \tag{46}$$

$$\lambda_{r2} = 2\sqrt{\frac{A_{rbp}}{\pi}} \tag{47}$$

Moreover, the side plane of RSPM is a regular triangle composed of three solid particles. Similarly, the area of the side plane of RSPM (A_{rs}) and the area of solid particles (A_{rss}) respectively are expressed as:

$$A_{rs} = \frac{\sqrt{3}}{4} L_{rl}^2 \tag{48}$$

$$A_{rss} = \frac{1}{2}\pi R_v^2 \tag{49}$$

Therefore, the area of pore in the side plane of RSPM (A_{rsp}) is given by:

$$A_{rsp} = \frac{\sqrt{3}}{4} L_{rl}^2 - \frac{1}{2}\pi R_v^2 \tag{50}$$

By approximating the irregular pore area in the side plane of RSPM, its diameter (λ_{r3}) can be calculated:

$$A_{rsp} = \pi\left(\frac{\lambda_{r3}}{2}\right)^2 \tag{51}$$

$$\lambda_{r3} = 2\sqrt{\frac{A_{rsp}}{\pi}} \tag{52}$$

Similarly, the gap length (ΔL_{rl}) between the adjacent particles in RSPM is given by:

$$\Delta L_{rl} = L_{rl} - 2R_v = R_v\left(\sqrt[3]{\frac{8\pi}{3(1-n)}} - 2\right) \tag{53}$$

The average diameter length of the capillary tube in RSPM (λ_r) is calculated as:

$$\lambda_r = \frac{\lambda_{r1} + \lambda_{r2} + \lambda_{r3} + \Delta L_{rl}}{4} \tag{54}$$

Besides, the total volume of the right square pyramid in RSPM microstructure is $V_r = \frac{\sqrt{2}}{6} L_{rl}^3 = \frac{\sqrt{2}}{6}(2R_v + \Delta L_{rl})^3$ and the inner pore volume is $V_{rp} = V_r - \frac{4}{9}\pi R_v^3 = \frac{\sqrt{2}}{6}(2R_v + \Delta L_{rl})^3 - \frac{4}{9}\pi R_v^3$. Therefore, the porosity of RSPM is given by:

$$n = \frac{V_{rp}}{V_r} = \frac{\frac{\sqrt{2}}{6}(2R_v + \Delta L_{rl})^3 - \frac{4}{9}\pi R_v^3}{\frac{\sqrt{2}}{6}(2R_v + \Delta L_{rl})^3} \tag{55}$$

The ratio $p_1 = \Delta L_{tl}/R_v$ of RSPM is obtained by solving Eq. 56:

$$p_1 = \frac{\Delta L_{rl}}{R_v} = 2\sqrt[3]{\frac{\pi}{3\sqrt{2}(1-n)}} - 2 \tag{56}$$

Afterward, the tortuosity of RSPM can be quantified by Eq. 30. Similarly, the dimensionless pore volume of the right square pyramid in RSPM microstructure (Fig. S1c) is given by:

$$V_{rp} = \left(L_{rl}^+\right)^{D_f} \tag{57}$$

where $L_{rl}^+ = L_{rl}/d_{\min}$. D_f is achieved from Eq. 58:

$$D_f = \frac{\ln V_{rp}}{\ln L_{rl}^+} \tag{58}$$

The dimensionless total volume of the right square pyramid in RSPM (V_r^+) is given by:

$$V_r^+ = \frac{V_r}{V_{sp}} = \frac{V_r}{\frac{1}{6}\pi d_{\min}^3} \tag{59}$$

Simultaneously, the dimensionless total volume of the right square pyramid in RSPM (V_r^+) can be written as:

$$V_r^+ = \left(L_{rl}^+\right)^3 \tag{60}$$

Afterward, L_{rl}^+ is calculated as:

$$L_{rl}^+ = \sqrt[3]{V_r^+} = d^+ \sqrt[3]{\frac{1}{3(1-n)}} \tag{61}$$

Consequently, the D_f of RSPM is derived as:

$$\begin{aligned} D_f &= \frac{\ln V_{rp}}{\ln L_{rl}^+} = \frac{\ln\left(V_r^+ n\right)}{\ln \sqrt[3]{V_r^+}} \\ &= 3 + \frac{\ln n}{\ln L_{rl}^+} \\ &= 3 + \frac{\ln n}{\ln\left[d^+ \sqrt[3]{\frac{1}{3(1-n)}}\right]} \end{aligned} \tag{62}$$

The capillary pressure of tortuous capillary tubes (P_c) can be quantified based on Yong-Laplace equation [62]:

$$P_c = \frac{\omega}{\lambda}\frac{1-n}{n} \tag{63}$$

where λ is the diameter of capillary tube; $\omega = F\sigma\cos\theta$; θ is the contact angle at the interface between fluid phase and solid phase; σ is the surface tension of fluid; F is the form factor related to capillary tube alignment and flow direction.

2.2. Sequential Gaussian simulation

SGS is used to generate heterogeneous porosity fields of an idealized granular aquifer to determine the effects of RTM and RSPM on DNAPL migration and remediation. Kriging is used to supply the mean and variance for conditional distributions in SGS when all distributions follow a normal distribution. SGS transforms observation data into a Gaussian distribution, after which a simple kriging estimation system is applied to simulate using the semivariogram model. Previous research suggests that 50–400 realizations are necessary to achieve a statistically stable mean realization [63,64]. This study examines the influence of microstructure on DNAPL behavior by generating 200 porosity fields for an idealized aquifer comprised of granular porous media.

2.3. Numerical simulation of DNAPL migration and remediation

UTCHEM (University of Texas Chemical Compositional Simulator) is a multicomponent, multiphase model simulator applied to simulate the migration and remediation of DNAPL in the idealized heterogeneous aquifer [65]. There is no limit to the number of chemical components that can be specified by the user in UTCHEM, including water, organic contaminants, surface active agents, alcohols, polymers, chloride, calcium, other electrolytes, microbiological species, electron acceptors, etc. Chemical reactions, dispersion, diffusion, adsorption, capillary pressures, and mass transfer between phases are all included in UTCHEM. UTCHEM is particularly useful for environmental applications, such as SEAR.

3. Application to a synthetic heterogeneous PCE-contaminated site

An idealized aquifer consists of different grades of sand, whose properties are shown in Table S1 from related references. The particles of sand conform to the microstructural model developed in this study. Aquifer a, as shown in Fig. 1a, has a rectangle area of 100 m × 51 m and a depth of 26 m, divided into 25 (X axis) × 17 (Y axis) × 13 (Z axis) girds, each with dimensions of 4 m × 3 m × 2 m. There are no-flow boundaries at the top and bottom of the aquifer, while the left and right borders are constant potential boundaries with groundwater flows from left to right (hydraulic gradient is 0.005 m/m). Six injection wells and six extraction wells are installed to remediate the groundwater contaminant by the SEAR technique (Fig. 1b). The SEAR technique utilizes six injection wells and six extraction wells to remediate the groundwater contamination. All injection and extraction wells penetrate the entire depth of the aquifer.

The idealized aquifer has a porosity following a normal distribution (mean is 0.22, standard deviation is 0.07). The correlation length of 5 m is set for both the horizontal and vertical directions of the porosity distribution. As shown in Fig. 2a, one of the 200 realizations of the porosity field is generated by SGS methods in the GSLIB program, and corresponding statistical analysis is performed (Fig. 2f). According to Fig. 2f, the frequency distribution of the single realization follows Gaussian distribution, which is the most popular distribution of variables in nature [66]. RTM and RSPM permeability distributions are derived by Eq. 11 from the associated parameters D_t, D_f and the diameter of the capillary tube (Fig. 2b and c). The porosity field follows a normal distribution (Fig. 2f), whereas the permeability field follows a lognormal distribution (Fig. 2g and h). The phenomenon is consistent with previous findings that aquifer penetration parameters are largely characterized by lognormal distributions [66,67]. Simultaneously, both RTM and RSPA

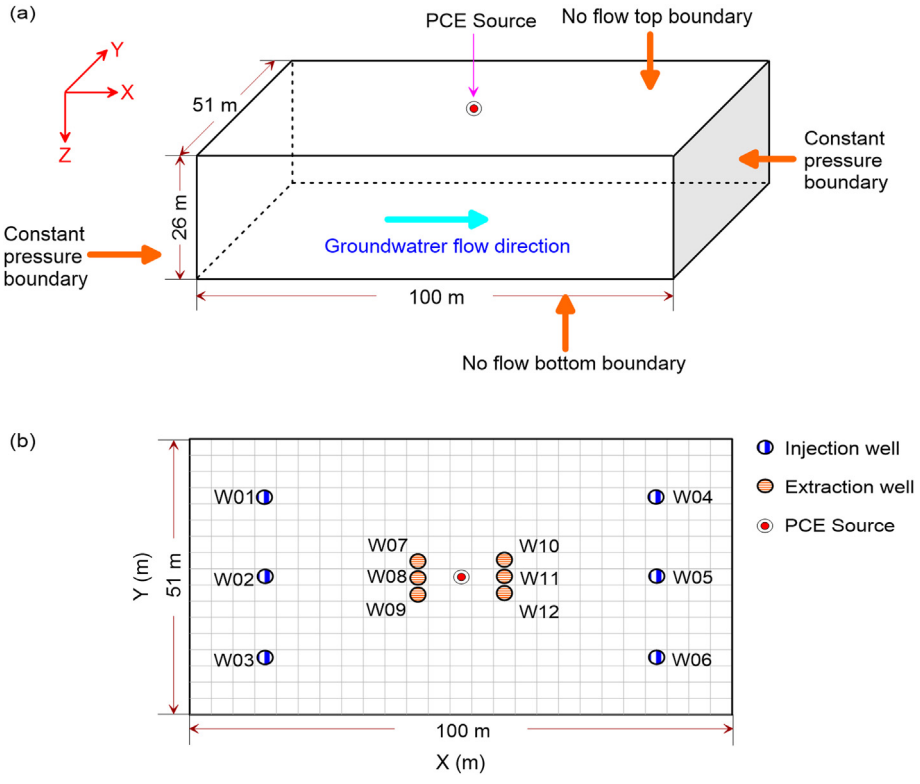

Fig. 1. Idealized aquifer composed of granular porous media and boundary conditions (a); set of injection and extraction wells used for contamination remediation (b).

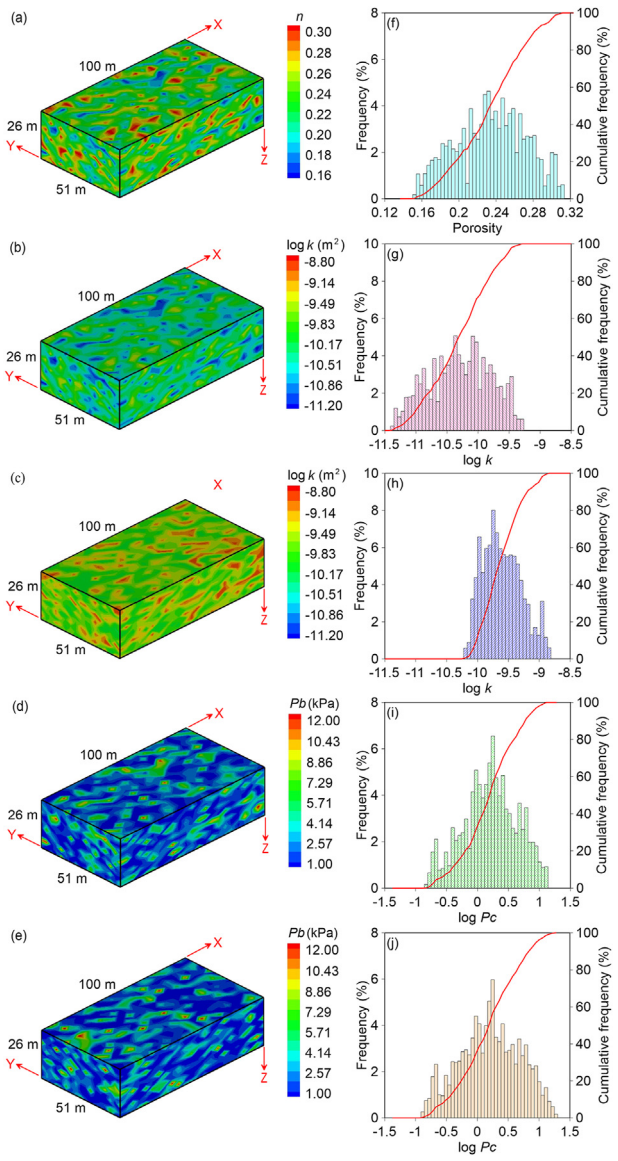

Fig. 2. Individual porosity field (a), permeability fields of RTM (b) and RSPM (c), entry pressure fields of RTM (d) and RSPM (e), and corresponding statistical analysis results (f–j).

exhibit some differences in their permeability fields. The mean values of individual permeability realizations of RTM and RSPM are 5.430×10^{-11} m^2 and 2.493×10^{-10} m^2, respectively. Furthermore, the mean values of 200 permeability realizations of RTM and RSPM are 8.360×10^{-11} m^2 and 2.643×10^{-10} m^2, which indicates the permeability of RSPM is larger than that of RTM.

According to Eqs. 27 and 55 for RTM and RSPM, their median pore diameters are determined. Using Eq. 63, entry pressures for RTM and RSPM can be calculated. In detail, the individual realization of entry pressure for RTM is illustrated in Fig. 2d, and the corresponding frequency is illustrated in Fig. 2i. Simultaneously, the individual realization of entry pressure and associated frequency for RSPM is shown in Fig. 2e and j, respectively. Lognormal distributions are observed for both entry pressure distributions of RTM and RSPM. RTM and RSPM have average entry pressures of 1.313 kPa and 1.449 kPa for the single realization, indicating RSPM has a slightly higher entry pressure. RTM and RSTM have no apparent difference in the frequency of entry pressure distribution (Fig. 2i and j), but RSTM and RSPM have quite different permeability frequencies (Fig. 2g and h). Therefore, microstructure has a significant impact on aquifer characteristics, which will ultimately affect associated water and contaminant transfer. The microstructure of porous media plays a significant role in permeability, while entry pressure is only slightly affected.

As a result of a contamination spill event, the underground storage tank at the top of the granular aquifer leaks PCE into the subsurface environment. To clean up PCE contamination, SEAR is applied after PCE migrates freely for a long time. There are four stages in the entire migration and remediation of PCE systems. Firstly, the underground storage tank at the center grid block of the top layer spills 300 m^3 of PCE into the aquifer every day at a rate of 10.00 m^3/day. The PCE spill period lasts 30 days, after which the underground storage tank does not releases any PCE into the aquifer during day 30 to day 100. Afterward, six injection wells are injected with 4% surface active agent solution at a rate of 43.00 m^3/day for t = 100–150 days. Simultaneously, the extraction rate of six extraction wells is also 43.00 m^3/day. The relative permeability of both oil (DNAPL) and water phases increases in the presence of surfactant, while viscosity and capillary pressure are reduced by surfactant. This is a result of the surfactant lowering the interfacial tension, resulting in lower residual oil saturation and bound water saturation [9, 65,68]. Therefore, surface active agents can solubilize and mobilize DNAPL in groundwater systems, after which DNAPL is extracted through an extraction well from the aquifer. The contaminated aquifer is then flushed with water for 150 days to sufficiently remove the DNAPL. The PCE migration and remediation can be generalized to a three-dimensional, unsteady, multiphase flow problem in the heterogeneous aquifer, which is simulated by UTCHEM [65] to investigate the influence of the microstructure of porous media on macroscopic PCE transport and SEAR efficiency. The parameters related to numerical simulation are illustrated in Fig. 2a–e and Table S2.

4. Results and discussion

4.1. Single realization

3D visualizations of the PCE plume and 2D visualizations in the vertical section plane during the entire migration and SEAR periods are shown in Fig. 3. Since PCE has a greater density than groundwater, it migrates through the aquifer from the upper to the lower layers and expands the contamination plume (Fig. 3a and b). As the migration progressed, PCE plume is slightly inclined in the direction of horizontal groundwater flow (Fig. 3c). Due to heterogeneity in porosity, permeability, and entry pressure, PCE spreads irregularly in aquifers and is entrapped in zones with high permeability and low entry pressure. Therefore, residual ganglia and globules are formed in the aquifer with RTM. There is a no-flow boundary at the bottom of the aquifer, which causes PCE to accumulate at the bottom and form a large pool after long-term migration (Fig. 3c).

In comparison with the simulated results of RTM (Fig. 3a–c), the PCE transport phenomenon in aquifers with RSPM is similar (Fig. 4a–c). Nevertheless, the transport of PCE in porous media is evidently affected by the difference in microstructures. Based on the results in Fig. 2, it appears that porous media with RSPM have much higher permeability (average permeability is 2.493×10^{-10} m^2) than that of RTM (average permeability is 5.430×10^{-11} m^2) under the same conditions. Simultaneously, both RTM and RSTM exhibit similar frequencies of entry pressure distribution. Therefore, PCE spreads more quickly in the aquifer with RSPM due to its greater mobility. The bottom PCE pool for RSPM has a greater maximum lateral extent than that of RTM (Figs. 3f–h and 4f–h). Additionally, PCE plume in aquifers with RSPM is also inclined with a larger inclination angle along the groundwater flow direction (Figs. 3 and 4).

After PCE migrates in groundwater over 100 days, SEAR is used to remove it. Simulation results of SEAR of single realizations for RTM during t = 100–300 days are shown in Fig. 3c–e and h–j. The remediation effect is not apparent during the first t = 100–150 days, possibly because most PCE is in the pool state during this period (Fig. 3d). Afterward, PCE

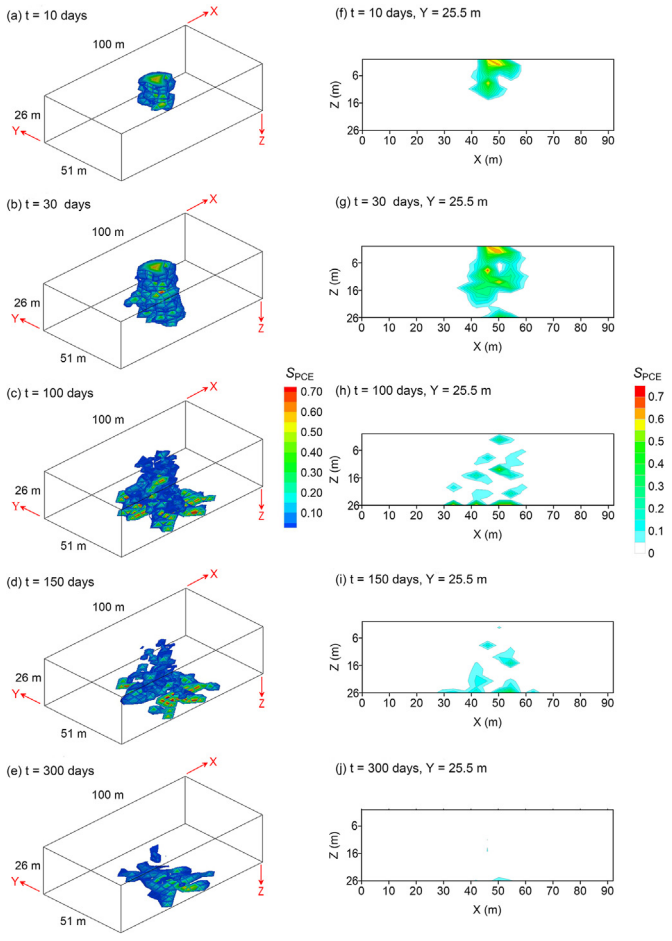

Fig. 3. Simulated PCE saturation of single realization for RTM during long-term migration and remediation periods (0–300 day): PCE plumes in 3D space at t = 10 days, 30 days, 100 days, 150 days and 300 days (a–f), respectively; corresponding PCE plume in the vertical section plane (Y = 25.5 m) at different times (e–j).

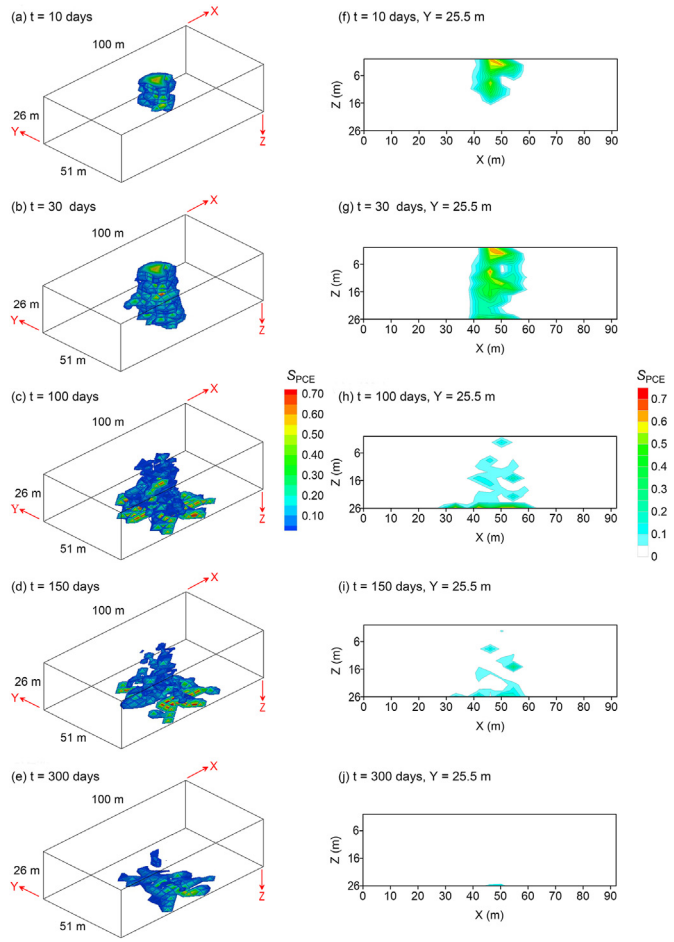

Fig. 4. Simulated PCE saturation of single realization for RSPM during long-term migration and remediation periods (0–300 day): PCE plumes in 3D space at t = 10 days, 30 days, 100 days, 150 days and 300 days (a–f), respectively; corresponding PCE plume in the vertical section plane (Y = 25.5 m) at different times (e–j).

remediation by SEAR is promoted by the formation of more residual ganglia and globules. During the water-flooding period, the PCE volume is significantly reduced, which indicates that PCE has been effectively removed from the contaminated aquifer (Fig. 3e and j). A total of 236.335 m^3 PCE is removed at t = 300 days, resulting in a remediation efficiency of 78.939%.

Fig. 4c–e presents the simulation results of SEAR for a single realization of RSPM. When t = 150 days, 162.3538 m^3 of PCE were removed, and remediation efficiency was 54.216% (Fig. 4d). The long-term remediation resulted in the removal of nearly 257.921 m^3 PCE and a remediation efficiency of 86.129%. Compared to RTM, PCE is easier to clean up in aquifers with RSPM, and less PCE remains in the groundwater system, resulting in a lower residual PCE volume (Fig. 4d and e). Simulation results show a clear correlation between microstructure and macroscopic PCE remediation. It is difficult to remove PCE from the aquifer with RTM using SEAR, whereas PCE can be removed more efficiently from the aquifer with RSPM.

4.2. Numerous SGS realizations

RTM and RSPM simulations are also performed for 200 realizations generated by the SGS method. PCE volumes in the aquifer increase linearly with time during the first t = 0–30 days (Fig. 5a). The remaining PCE volumes after long-term SEAR for RTM and RSPM are 23.305–101.434 m^3 with a mean of 46.900 m^3 and 15.644–89.411 m^3 with a mean of 32.570 m^3, respectively. Besides, PCE infiltrates in aquifers with RSPM at a faster rate along the vertical direction (Fig. 4g). Compared to the residual PCE volumes in aquifers of RSPM, PCE remediation is difficult in the aquifer with RTM. When surface active agents are injected into the aquifer to remove PCE from porous media at t = 100 days and end at t = 150 days, the value of ganglia-to-pool ratio (GTP) shows an obvious variation (Fig. 5b). This phenomenon indicates that surface active agent is capable of influencing GTP values of PCE plume. A decrease in GTP is followed by an increase in GTP during the water-flushing period, which suggests the architecture of the PCE plume changes during the water-flushing processes. At t = 300 days, GTP values are 0.183–1.365 (average value is 0.873) and 0.227–1.229 (average value is 0.898) for RTM and RSPM, respectively. The relationship between cumulative PCE removal rate and remediation time is presented in Fig. 5c and the relationship between GTP value and cumulative PCE removal rate is presented in Fig. 5d.

After the surface active agent injection period, there is still some PCE remaining in the aquifer. The residual PCE in groundwater is then cleaned up by following water-flushing process (Fig. 5c). At t = 300 days, the cumulative PCE removal volumes of RTM and RSPM reach 198.037–276.002 m^3 (mean value is 252.292 m^3) and 210.117–283.666 m^3 (mean value is 266.852 m^3), corresponding to remediation efficiency of 66.129%–92.214% (mean values is 84.324%) and 70.149%–94.773% (mean value is 89.122%), respectively. In comparison with RTM, SEAR has a higher remediation efficiency for aquifers with RSPM, suggesting it is easier to clean up contaminated aquifers with RSPM. Fig. 5d shows that GTP values are relatively low before 50% PCE

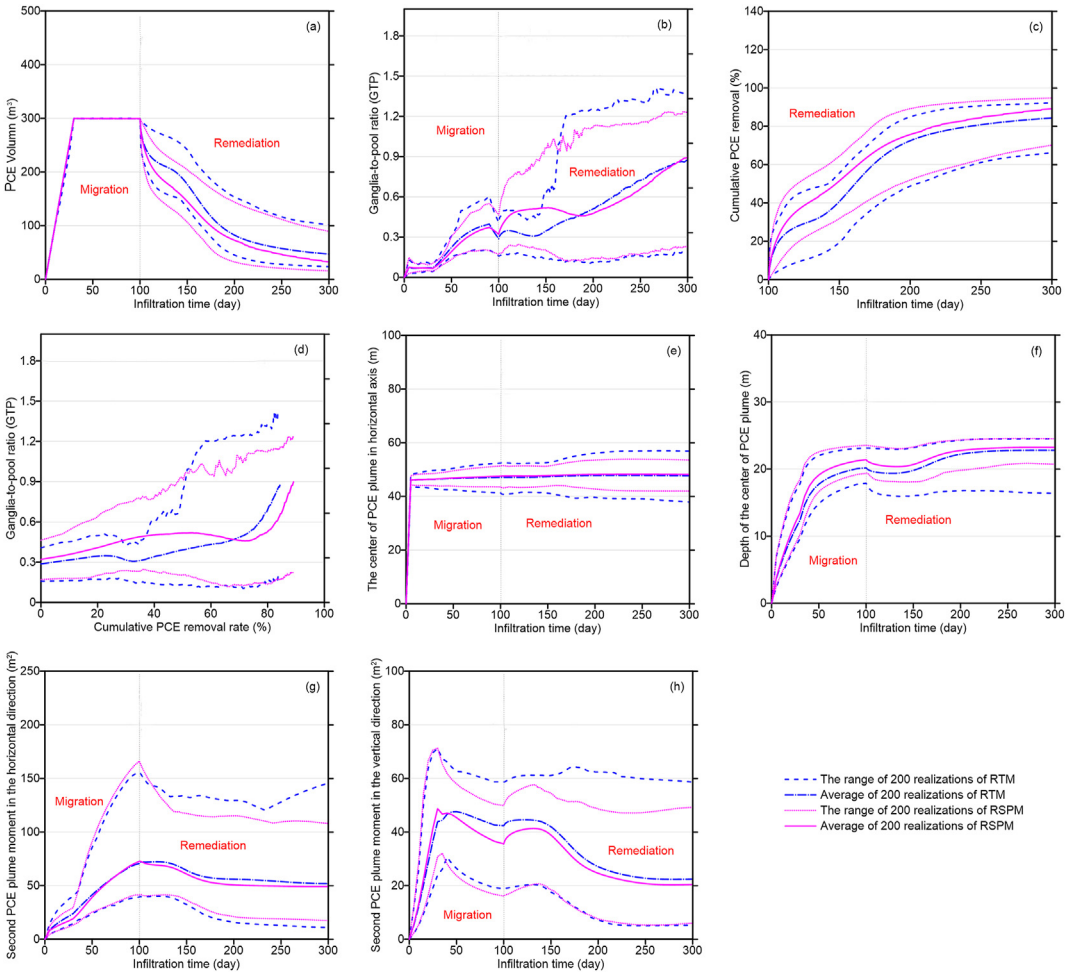

Fig. 5. The change of PCE volume contained in idealized aquifer over entire migration and remediation periods (a); changes in GTP of PCE plume (b); cumulative PCE removal rate as time goes on (c); GTP value as a function of cumulative PCE removal rate (d); the center of PCE plume in horizontal axis versus time (e); vertical depth of the center of PCE plume versus time (f); second moment of PCE plume in the horizontal direction versus time (g); second moment of PCE plume versus time in vertical direction (h).

is removed from the aquifer. After 50% of PCE is removed from the aquifer, the GTP value increases as more PCE are transformed from pool to ganglia state. After most of the PCE is cleaned up, GTP continuously increases again due to the small pool of PCE remaining at the bottom of the aquifer.

As shown in Fig. 5e–h, the first and second moments of the PCE plume are obtained through moment analysis. For RTM and RSPM, the PCE plume centers are very close to each other along a horizontal direction (Fig. 5e). According to Fig. 2, the permeability of porous media obtained by RSPM is higher than that of RTM. As a result, the PCE plume expands more easily and contaminates the aquifer more extensively in the aquifer with RSPM. Furthermore, PCE can be more easily removed from the aquifer with RSPM using SEAR. During t = 0–100 days (migration period), PCE plumes in aquifers with RSPM have a smaller second moment in the horizontal direction than that in aquifers with RTM, which may be caused by the larger transport capacity of PCE in the aquifer with RSPM. During t = 100–300 days (SEAR period), the remediation efficiency obtained by RSPM is higher than that obtained by RTM because PCE is easier to remove in the aquifer with RSPM. Consequently, the second moments along the horizontal direction for RTM and RSPM are 10.896–145.660 m^2 (mean value is 51.825 m^2) and 17.598–108.000 m^2 (mean value is 49.195 m^2) at t = 300 days, which indicates RTM has slightly larger values of the second moments along the horizontal direction (Fig. 5g). At t = 300 days, PCE plume centers are similar along the vertical direction for RTM and RSPM, while the plume extent obtained by RTM is larger than that obtained by RSPM (Fig. 5f). What's more, second moments along vertical direction for 200 realizations of RTM and RSPM are 18.837–153.170 m^2 (mean value is 65.766 m^2) and 27.344–133.040 m^2 (mean value is 69.529 m^2), respectively (Fig. 5h). Combining the second moments along horizontal and vertical directions, PCE plume area in aquifer with RSPM is larger than that of RTM, implying RSPM can cause a wider contamination plume.

Significantly, PCE is a typical DNAPL contaminant with a larger density compared with water, so the conclusions of this study are applicable to other similar DNAPL contaminants. However, other pollutants, such as light non-aqueous phase liquid (LNAPL) contaminants, have smaller densities compared with DNAPL and water. If other LNAPL contaminants are selected, the migration and remediation will be changed. The effects of 3D microstructure on the transport and remediation of other different contaminants in heterogeneous porous media are beyond this study and will be explored in our future research.

5. Conclusions

To investigate the influence of the microstructure of granular porous media on macroscopic contaminant migration and remediation, the fractal models are developed to quantify the macroscopic parameters (such as porosity, permeability, and entry pressure) for two 3D microstructures of porous media-RTM and RSPM. Using the SGS method, 200

realizations of an idealized aquifer composed of different grades of sand are generated. The long-term PCE transport and SEAR process is simulated by UTCHEM using distributions of porosity, permeability, and entry pressure derived from the fractal models of RTM and RSPM. Results suggest the mobility of PCE plume in aquifers with RTM is less than that in aquifers with RSPM. Simultaneously, PCE contamination is difficult to remove from aquifers with RTM by SEAR. After long-time SEAR remediation, the cumulative PCE removal rates are 66.129%–92.214% (mean value is 84.324%) for 200 realizations of RTM, and 70.149%–94.773% (mean value is 89.122%) for 200 realizations of RSPM, respectively. Moreover, The GTP of the PCE plume obtained by RSPM is mostly higher than that obtained by RTM. Findings from this work suggest that the microstructure of granular porous media is fundamental to understanding aquifer characteristics and contaminant migration as well as remediation effects. Furthermore, the migration behavior of DNAPL and other organic pollutants (such as chlorobenzene, light non-aqueous phase liquid) in groundwater under different conditions (simulation factors are permeability coefficient and pressure), DNAPL remediation by other materials (such as oxidation agents and adsorption agents), and verification of 3D microstructure models of porous media by experiments and actual site research will be explored in our future research to provide recommendations for prediction and management of PCE migration.

CRediT authorship contribution statement

Zhou Cheng: Writing – original draft, Funding acquisition, Conceptualization. **Ming Wu:** Writing – review & editing, Writing – original draft, Project administration, Funding acquisition, Conceptualization. **Yanru Hao:** Methodology, Conceptualization. **Cehui Mo:** Methodology, Conceptualization. **Qusheng Li:** Methodology, Conceptualization. **Jianfeng Wu:** Methodology, Conceptualization. **Jichun Wu:** Methodology, Conceptualization. **Bill X. Hu:** Methodology, Conceptualization. **Guoping Lu:** Methodology, Conceptualization.

Declaration of competing interests

The authors declare that they have no known competing financial interests or personal relationships that could have appeared to influence the work reported in this paper.

Acknowledgments

This research was supported by the National Key Research and Development Plan of China (no. 2019YFC1804302), the Natural Science Foundation of Guangdong Province (no. 2023A1515012228) and Guangdong Provincial Environmental Protection Fund (Guangdong Financial Budget 2024 4).

Appendix A. Supplementary data

Supplementary data to this article can be found online at https://doi.org/10.1016/j.eehl.2024.08.003.

References

[1] J.A. Boswinkel, Information Note. International Groundwater Resources Assessment Centre (IGRAC), Netherland Institute of Applied Geoscience, Netherlands, 2000.
[2] J.E. Asuquo, E.E. Etim, Physicochemical and bacteriological studies of selected borehole water in uyo metropolis in akwa ibom state, Int. J. Mod. Chem. 2 (1) (2012) 7–14.
[3] M. Valipour, Comparison of surface irrigation simulation models: full hydrodynamic, zero inertia, kinematic wave, J. Agric. Sci. 4 (12) (2012) 68–74.
[4] M. Valipour, Future of agricultural water management in Africa, Arch. Agron Soil Sci. 61 (7) (2015) 907–927.
[5] S.I. Yannopoulos, G. Lyberatos, N. Theodossiou, W. Li, M. Valipour, A. Tamburrino, et al., Evolution of water lifting devices (pumps) over the centuries worldwide, Water 7 (2015) 5031–5060.
[6] M. Valipour, V.P. Singh, Global experiences on wastewater irrigation: challenges and Prospects, in: B. Maheshwari, V.P. Singh, B. Thoradeniya (Eds.), Balanced Urban Development: Options and Strategies for Liveable Cities. Volume 72 of the Series Water Science and Technology Library, 2016, pp. 289–327.
[7] Z. Demiray, N.H. Akyol, G. Akyol, N.K. Copty, Surfactant-enhanced in-situ oxidation of DNAPL source zone: experiments and numerical modeling, J. Contam. Hydrol. 258 (2023) 104233.
[8] E. Jeong, Y.I. Kim, J.Y. Lee, M. Raza, Microplastic contamination in groundwater of rural area, eastern part of Korea, Sci. Total Environ. 895 (2023) 165006.
[9] A. Alamooti, S. Colombano, A. Shoker, A. Ahmadi-Sénichault, F. Lion, D. Cazaux, et al., Enhancing remediation of residual DNAPL in multilayer aquifers: post-injection of alcohol-surfactant-polymer mixtures, Sci. Total Environ. 918 (2024) 170680.
[10] X.X. Kuang, J.G. Liu, B.R. Scanlon, J.J. Jiao, S. Jasechko, M. Lancia, et al., The changing nature of groundwater in the global water cycle, Science 383 (6686) (2024) eadf0630.
[11] P. Landrigan, R. Fuller, N.J.R. Acosta, O. Adeyi, R. Arnold, N. Basu, et al., The Lancet Commission on pollution and health, Lancet 391 (2018) 462–512.
[12] V.A. Bakshevskaia, S.P. Pozdniakov, Simulation of hydraulic heterogeneity and upscaling permeability and dispersivity in Sandy-Clay foormations, Math. Geosci. 48 (2016) 45–64.
[13] Q.L. Cui, H.N. Wu, S.L. Shen, Z.Y. Yin, S. Horpibulsuk, Protection of neighbour buildings due to construction of shield tunnel in mixed ground with sand over weathered granite, Environ. Earth Sci. 75 (2016) 458.
[14] H. Liu, Y.X. Li, X. He, Z. Sissou, L. Tong, C. Yarnes, et al., Compound-specific carbon isotopic fractionation during transport of phthalate esters in sandy aquifer, Chemosphere 144 (2016) 1831–1836.
[15] M. Wu, Z. Cheng, J.F. Wu, J.C. Wu, Quantifying representative elementary volume of connectivity for translucent granular materials by light transmission micro-tomography, J. Hydrol. 545 (2017) 12–27.
[16] S. Zhang, G.Z. Mao, J. Crittenden, X. Liu, H.B. Du, Groundwater remediation from the past to the future: a bibliometric analysis, Water Res. 119 (2017) 114–125.
[17] M. Cochennec, H. Davarzani, Y. Davit, S. Colombano, I. Ignatiadis, G. Masselot, et al., Impact of gravity and inertia on stable displacements of DNAPL in highly permeable porous media, Adv. Water Resour. 162 (2022) 104139.
[18] J.M. Bian, D.M. Ruan, Y. Wang, X.Q. Sun, Z.Q. Gu, Bayesian ensemble machine learning-assisted deterministic and stochastic groundwater DNAPL source inversion with a homotopy-based progressive search mechanism, J. Hydrol. 624 (2023) 129925.
[19] S.J. Guo, Y.Y. Zha, H. Zhong, X. Wang, D. Xu, Numerical investigations of influence on thermal conductive heating in DNAPL-impacted soils by heterogeneity, J. Hydrol. 258 (2023) 104232.
[20] S.A. Bradford, R.A. Vendlinski, L.M. Abriola, The entrapment and long-term dissolution of tetrachloroethylene in fractional wettability porous media, Water Resour. Res. 35 (10) (1999) 295–2964.
[21] L. Liu, Modeling for surfactant-enhanced groundwater remediation processes at DNAPLs-contaminated sites, J. Environ. Inform. 5 (2) (2005) 42–52.
[22] C. Carroll, K, K. McDonald, J. Marble, A.E. Russo, M.L. Brusseau, The impact of transitions between two-fluid and three-fluid phases on fluid configuration and fluid-fluid interfacial area in porous media, Water Resour. Res. 51 (2015) 7189–7201.
[23] H.I. Essaid, B.A. Bekins, I.M. Cozzarelli, Organic contaminant transport and fate in the subsurface: evolution of knowledge and understanding, Water Resour. Res. 51 (2015) 4861–4902.
[24] J.Q. Huang, J.A. Christ, M.N. Goltz, A.H. Demond, Modeling NAPL dissolution from pendular rings in idealized porous media, Water Resour. Res. 51 (2015) 8182–8197.
[25] Y. Liu, S. Wang, C.A. McDonough, M. Khairy, D.C.G. Muir, P.A. Helm, et al., Gaseous and freely-dissolved PCBs in the lower great lake based on passive sampling: spatial trends and air-water exchange, Environ. Sci. Technol. 50 (2016) 4932–4939.
[26] C.E. Schaefer, E.B. White, G.M. Lavorgna, M.D. Annable, Dense nonaqueous-phase liquid architecture in fractured bedrock: implications for treatment and plume longevity, Environ. Sci. Technol. 50 (2016) 207–213.
[27] T.S. Weathers, K. Harding-Marjanovic, C.P. Higgins, L. Alvarez-Cohen, J.O. Sharp, Perfluoroalkyl acids inhibit reductive dechlorination of Trichloroethene by repressing dehalococcoides, Environ. Sci. Technol. 50 (2016) 240–248.
[28] M. Wu, J.F. Wu, J.C. Wu, Simulation of DNAPL migration in heterogeneous translucent porous media based on estimation of representative elementary volume, J. Hydrol. 553 (2017) 276–288.
[29] Y. Wang, J. Bian, X. Sun, D. Ruan, Z. Gu, Sensitivity-dependent dynamic searching approach coupling multi-intelligent surrogates in homotopy mechanism for groundwater DNAPL-source inversion, J. Contam. Hydrol. 255 (2023) 104151.
[30] L.F. Chen, G.T. Ding, J. Lu, Y.X. Liu, S.M. Wei, X.J. Guo, et al., Gas tube effect: a transport mode of deeply buried volatile DNAPLs to shallow strata, J. Hydrol. 630 (2024) 130696.
[31] D.M. O'Carroll, S.A. Bradford, L.M. Abriola, Infiltration of PCE in a system containing spatial wettability variations, J. Contam. Hydrol. 73 (2004) 39–63.
[32] Z.Y. Hou, K. Zhao, S. Wang, Y. Wang, W.X. Lu, Bayesian hybrid-kernel machine-learning-assisted sensitivity analysis and sensitivity-relevant inverse modeling for groundwater DNAPL contamination, J. Hydrol. 633 (2024) 131009.
[33] C.G. Yang, C.P. Zhang, F.Y. Liu, J. Dong, Remediation of DNAPL-contaminated heterogeneous aquifers using colloidal biliquid aphron: multiscale experiments and pore-scale simulations, J. Hydrol. 628 (2024) 130532.
[34] M.M. Bob, M.C. Brooks, S.C. Mravik, A.L. Wood, A modified light transmission visualization method for DNAPL saturation measurements in 2-D models, Adv. Water Resour. 31 (2008) 727–742.

[35] C. Liang, M.C. Lai, Trichloroethylene degradation by zero valent iron activated persulfate oxidation, Envrion. Eng. Sci. 25 (7) (2008) 1071–1077.
[36] C. Liang, C.L. Hsieh, Evaluation of surfactant flushing for remediating EDC-tar contamination, J. Contam. Hydrol. 177–178 (2015) 158–166.
[37] S. Omirbekov, S. Colombano, A. Alamooti, A. Batikh, M. Cochennec, Y. Amanbek, et al., Experimental study of DNAPL displacement by a new densified polymer solution and upscaling problems of aqueous polymer flow in porous media, J. Contam. Hydrol. 252 (2023) 104120.
[38] J.X. Shi, X.H. Chen, B. Ye, Z.W. Wang, Y.Y. Sun, J.C. Wu, et al., A comparative study of DNAPL migration and transformation in confined and unconfined groundwater systems, Water Res. 245 (2023) 120649.
[39] M. Herraiz-Carboné, A. Santos, A. Checa-Fernández, C.M. Domínguez, S. Cotillas, Removal of organochlorine pollutants from DNAPL-saturated groundwater using electrolysis with MMO anodes, Chem. Eng. J. 486 (2024) 150238.
[40] B.M. Yu, J.H. Li, A geometry model for tortuosity of flow path in porous media, CHIN. Phys. Lett. 21 (2004) 1569–1571.
[41] B.M. Yu, Fractal character for tortuous streamtubes in porous media, Chin. Phys. Lett. 22 (2005) 158–160.
[42] Y.J. Feng, B.M. Yu, Fractal dimension for tortuous streamtubes in porous media, Fractals 15 (2007) 385–390.
[43] X.Y. Kang, C. Power, A. Kokkinaki, A. Revil, J.C. Wu, X.Q. Shi, et al., Characterization of DNAPL source zones in clay-sand media via joint inversion of DC resistivity, induced polarization and borehole data, J. Contam. Hydrol. 258 (2023) 104240.
[44] M.J. Yun, B.M. Yu, P. Xu, J.S. Wu, Geometrical models for tortuosity of streamlines in three-dimensional porous media, Can. J. Chem. Eng. 84 (2006) 301–309.
[45] L. Li, B.M. Yu, Fractal analysis of the effective thermal conductivity of biological media embedded with randomly distributed vascular trees, Int. J. Heat Mass Tran. 67 (2013) 74–80.
[46] J. Bear, Dynamics of Fluids in Porous Media, Soil Sci. 120 (2) (1975) 162–163.
[47] Y.Q. Shen, P. Xu, S.X. Qiu, B.Q. Rao, B.M. Yu, A generalized thermal conductivity model for unsaturated porous media with fractal geometry, Int. J. Heat Mass Tran. 152 (2020) 119540.
[48] P. Pfeifer, D. Avnir, Chemistry in Nonintegral dimensions between two and three. I . Fractal theory of heterogeneous surface, J. Chem. Phys. 79 (1983) 3558–3565.
[49] A.J. Katz, A.H. Thompson, Fractal sandstone: implications for conductivity and pore formation, Phys. Rev. Lett. 54 (1985) 325–332.
[50] C.E. Krohn, Sandstone fractal and Euclidean pore volume distributions, J. Geophys. Res. 93 (1988) 3286–3296.
[51] T. Kim, W.S. Han, S. Yoon, P.K. Kang, J.Y. Shin, M.J. Nam, Evaluation of the impact of transition from porous to fractured rock media on 3D field-scale DNAPLs contamination, J. Hazard Mater. 462 (2024) 132711.
[52] B.M. Yu, P. Cheng, Fractal models for the effective thermal conductivity of bidispersed porous media, J. Thermophys. Heat Tran. 16 (2002) 22–29.
[53] B.M. Yu, J.C. Cai, M.Q. Zou, On the physical properties of apparent two-phase fractal porous media, Vadose Zone J. 8 (2009) 177–186.
[54] J.C. Cai, B.M. Yu, M.Q. Zou, M.F. M, Fractal analysis of invasion depth of extraneous fluids in porous media, Chem. Eng. Sci. 65 (2010) 5178–5186.
[55] S.S. Yang, R.K. Cui, X.B. Yuang, M.Q. Zou, Fractal study on permeability characteristics in rough and dense porous media, Chem. Eng. Sci. 282 (2023) 119265.
[56] X. Yang, Y.P. Du, Q. Xu, F.T. Wu, T. Zhou, C.Y. Zhao, Pores integrated fractal (PIF) analysis on transportation in porous media considering spatial distribution of pores and genuine tortuosity, Int. J. Heat Mass Tran. 187 (2022) 122528.
[57] M. Wu, J.F. Wu, J.C. Wu, B.X. Hu, Effects of microarrangement of solid particles on PCE migration and its remediation in porous media, Hydrol. Earth Syst. Sci. 22 (2) (2018) 1001–1015.
[58] M. Wu, J.F. Wu, J.C. Wu, B.X. Hu, A new criterion for determining the representative elementary volume of translucent porous media and inner contaminant, Hydrol. Earth Syst. Sci. 24 (12) (2020) 5903–5917.
[59] M. Wu, Z. Cheng, G.P. Lu, C.H. Mo, Y.R. Hao, Q.S. Li, et al., Impact of grain geometry on chlorohydrocarbon contaminant transformation and reductive dichlorination activity, J. Petrol. Sci. Eng. 229 (2023) 212143.
[60] A. Koponen, M. Kataja, J. Timonen, Tortuous flow in porous media, Phys. Rev. E 54 (1996) 406–410.
[61] O.O. Taiwo, D.P. Finegan, D.S. Eastwood, J.L. Fife, L.D. Brown, J.A. Darr, et al., Comparison of three-dimensional analysis and stereological techniques for quantifying lithium-ion battery electrode microstructures, J. Microsc. 263 (3) (2016) 280–292.
[62] K.J. Ahn, J.C. Seferis, Simultaneous measurements of permeability and capillary pressure of thermosetting matrices in woven fabric reinforcements, Polym. Composite. 12 (1991) 146–152.
[63] J.R. Eggleston, S.A. Rojstaczer, J.J. Peirce, Identification of hydraulic conductivity structure in sand and gravel aquifers: cape Cod data set, Water Resour. Res. 32 (1996) 1209–1222.
[64] K. Hu, R. White, D. Chen, B. Li, W. Li, Stochastic simulation of water drainage at the field scale and its application to irrigation management, Agric. Water Manag. 89 (2007) 123–130.
[65] M. Delshad, G.A. Pope, K. Sepehrnoori, A compositional simulator for modeling surfactant enhanced aquifer remediation, 1 Formation, J. Contam. Hydrol. 23 (1996) 303–327.
[66] R.H. Montgomery, J.C. Loftis, J. Harris, Statistical characteristics of ground-water quality variables, Ground Water 25 (2) (1987) 176–184.
[67] D. Veneziano, A. Tabaei, Nonlinear spectral analysis of flow through porous media with isotropic lognormal hydraulic conductivity, J. Hydrol. 294 (2004) 4–17.
[68] Z.J. Wang, Z.B. Yang, R. Hu, Y.F. Chen, Mass transfer during surfactant-enhanced DNAPL remediation: pore-scale experiments and new correlation, J. Hydrol. 621 (2023) 129586.